SAND2022-6901J

Design and Characterization of an Optically-Segmented Single Volume Scatter Camera Module

Kevin Keefe, Hassam Alhajaji, Erik Brubaker, *Member, IEEE*, Andrew Druetzler, Aline Galindo-Tellez, John Learned, Paul Maggi, *Member, IEEE*, Juan J.Manfredi, Kurtis Nishimura, *Member, IEEE*, Bejamin Pinto Souza, John Steele, Melinda Sweany, Eric Takahashi

***Abstract*—The Optically Segmented Single Volume Scatter Camera (OS-SVSC) aims to image neutron sources for nuclear non-proliferation applications using the kinematic reconstruction of elastic double-scatter events. We report on the design, construction, and calibration of one module of a new prototype. The module includes 16 EJ-204 organic plastic scintillating bars individually wrapped in Teflon tape, each measuring 0.5 cm $\times$ 0.5 cm $\times$ 20 cm. The scintillator array is coupled to two custom Silicon Photomultiplier (SiPM) boards consisting of a 2×8 array of SensL J-Series-60035 Silicon Photomultipliers, which are read out by a custom 16 channel DRS-4 based digitizer board. The electrical crosstalk between SiPMs within the electronics chain is measured as $0.76\% \pm 0.11\%$ among all 16 channels. We report the detector response of one module including interaction position, time, and energy, using two different optical coupling materials: EJ-560 silicone rubber optical coupling pads and EJ-550 optical coupling grease. We present results in terms of the overall mean and standard deviation of the z-position reconstruction and interaction time resolutions for all 16 bars in the module. We observed the 1σ z-position resolution for gamma interactions in the 0.3 MeVee to 0.4 MeVee range to be 2.24 cm $\pm$ 1.10 cm and 1.45 cm $\pm$ 0.19 cm for silicone optical coupling pad and optical grease, respectively. The observed 1σ interaction time resolution is 265 ps $\pm$ 29 ps and 235 ps $\pm$ 10 ps for silicone optical coupling pad and optical grease, respectively.**

***Index Terms*—fast neutron imaging, special nuclear material detection**

I. Introduction

The Single Volume Scatter Camera (SVSC) project aims to develop a portable kinematic neutron imaging system [1]. In comparison to conventional neutron scatter camera implementations [2–6], a compact scintillator geometry is used to reconstruct multiple neutron interactions, rather than distributed volumes. It is estimated that a single-volume neutron scatter camera with an interaction resolution of $O(1\,\mathrm{cm}, 1\,\mathrm{ns})$ can result in an order of magnitude improvement in detection efficiency compared to traditional designs [7], in addition to improvements in size, weight, and power of the instrument. Reduced system size enhances the practicality of the device in the field and also enables additional performance boosts via closer physical distance to objects of interest.

Kevin Keefe (email: kevinpk@hawaii.edu), Hassam Alhajaji, Andrew Druetzler, John Learned, Kurtis Nishimura, Bejamin Pinto Souza, and Eric Takahashi are with University of Hawaii, Manoa HI 96826 USA.

Aline Galindo-Tellez was with University of Hawaii, Manoa HI 96826 USA and is now with Institut de recherche sur les lois Fondamentales de l'Univers, CEA, Université Paris-Sacley, 91191.

Erik Brubaker, Melinda Sweany, and John Steele are with Sandia National Laboratories, CA 94550.

Paul Maggi was with with Sandia National Laboratories, CA 94550 USA and is now with Lawrence Livermore National Laboratories 94550 USA.

Juan Manfredi was with the University of Berkeley, CA 94720 USA and is now with Air Force Institute of Technology at Wright-Patterson Air Force Base in Ohio 45433 USA.

The authors thank the US DOE National Nuclear Security Administration, Office of Defense Nuclear Nonproliferation Research and Development for funding this work.

This material is based upon work supported by the U.S. Department of Energy, National Nuclear Security Administration through the Nuclear Science and Security Consortium under Award DE-NA0003180.

The SVSC relies on accurately reconstructing the time, position, and energy of two neutron-proton interactions within the compact volume of scintillator. The reconstruction of the incoming neutron direction is dependent on the incoming neutron energy, E_n, and the energy after the first interaction $E_{n'}$:

$$\cos(\theta) = \sqrt{\frac{E_{n'}}{E_n}}\,. \tag{1}$$

The quantity $E_{n'}$ is determined by the neutron time-of-flight equation, requiring knowledge of the position and time of the first two neutron-proton interactions:

$$E_{n'} = \frac{1}{2} m_n \left(\frac{\Delta d}{\Delta t}\right)^2. \tag{2}$$

Finally, E_n is determined by the sum of $E_{n'}$ and the recoil energy of the proton from the first interaction, which is found using the proton light yield relation of the scintillator material [8].

The two main design concepts approached within the SVSC framework are monolithic and optically segmented designs. Monolithic compact designs propose to reconstruct multiple interaction positions within a single block of scintillator [7, 9]. In contrast, optically segmented (OS) approaches [10–14] employ an array of rectangular scintillator bars that are read out on both sides: for each interaction, the interaction time and position within the bar are reconstructed, while the other two dimensions are determined by which bar the scintillation event occurred in. Current methods to reconstruct the position along the bar include the log of the ratio of amplitudes at the two readout ends and the difference in pulse time arrival at the two ends. The performance of these position and time reconstruction methods depends on the properties of the scintillator and any reflective wrapping [15, 16].

Other optically segmented detection systems also try to optimize energy, timing, and position resolution of interactions within scintillator volumes. One example is Time-of-Flight Positron Emission Tomography (TOFPET) systems, which commonly use inorganic scintillators for higher light output and since gamma interactions are of interest. Recent work in commercial TOFPET has improved time-of-flight resolution values, which approach $200\,\mathrm{ps}$ due to recent improvements in SiPM arrays [17]. Another similar detector concept is neutrino directional detection systems, which also benefit from good energy resolution and higher energy range sensitivities. One difference is that, because neutrino cross-sections are so low, maximizing detector volume is a crucial design consideration. However, recent progress has been made towards smaller segmented ($9\,\mathrm{L}$) antineutrino imaging designs that also rely on dual-ended readout of SiPMs (see e.g. [18]).

Based on our study of different scintillator materials and reflective wrappings, we previously constructed a prototype OS-SVSC system with $0.5\,\mathrm{cm} \times 0.5\,\mathrm{cm} \times 20\,\mathrm{cm}$ EJ-204 scintillator bars wrapped in Teflon tape, read out by two commercially available ArrayJ-60035-64P-PCB Silicon Photomultiplier (SiPM) arrays from SensL. The full description of that system and its performance are reported in [11].

The prior OS system was affected by electrical crosstalk at the $10\,\%$ level within the electronics chain and the SiPM array itself, which is expected to negatively affect interaction reconstructions, as crosstalk from one neutron interaction could bias the time and energy measurements of the other interaction. Further tests demonstrated that crosstalk in the commercial SiPM array occurs primarily in quadrants, suggesting that one large contributor to this crosstalk is the SAMTEC connector (QTE-040-03) [11].

In addition to electrical crosstalk, the prior OS system was also likely affected by optical crosstalk between bars and suboptimal light collection due to the $0.5\,\mathrm{mm}$ thick EJ-560 silicone rubber optical coupling pads. A $0.5\,\mathrm{mm}$ stand-off between the scintillator and the SiPMs, which are separated by $0.2\,\mathrm{mm}$ within the ArrayJ-60035-64P-PCB, is likely to cause some optical crosstalk, even with the individually cut $5\,\mathrm{mm} \times 5\,\mathrm{mm}$ silicone optical pads used in the prototype. In addition, light escaping the edges of the pad can result in light loss, leading to degradation of resolution. Misalignment of the bars due to non-uniform Teflon wrapping is another potential source of optical crosstalk and light loss.

Detailed characterization of each bar in the prior 8×8 array was a challenge. Prior single-bar characterizations of the interaction time, energy, and position resolution were achieved with back-to-back $0.511\,\mathrm{MeV}$ annihilation gamma rays from a ^{22}Na source: using a tag scintillator with a known position along the bar, the position-dependent response was measured [15]. However, for bars near the center of a full array, this was difficult to achieve due to scattering in the outside bars. Thus, the inner bars of the prototype were characterized by using the outer bar position calibration to reconstruct individual cosmic muon tracks within the array, a time-consuming process.

We designed a second prototype based on the lessons learned in deploying and characterizing this prior prototype. Many of the engineering and detector characterization difficulties have been addressed by employing a modular design in which the detector can be split into multiple 2×8 scintillator arrays. We designed a custom SiPM array, which allowed for extra care in avoiding optical and electronic crosstalk: the pixels are separated by $2\,\mathrm{mm}$, rather than $0.2\,\mathrm{mm}$, so that optical crosstalk is more easily avoided, and the circuit was designed specifically to minimize electronic crosstalk between channels. The board is designed to interface directly with the Sandia Laboratories Compact Electronics for Modular Acquisition (SCEMA) electronics board [19]. Finally, the modular design assures that each bar is accessible for calibrations using a tagged ^{22}Na source.

II. Module Design

As stated above, the second OS-SVSC prototype uses a modular design to minimize electrical and optical crosstalk, and to enable faster and more accurate detector characterizations. A single Optically Segmented MOdule (OSMO) includes a total of sixteen $0.5\,\mathrm{cm} \times 0.5\,\mathrm{cm} \times 20\,\mathrm{cm}$ EJ-204 scintillator bars [20] configured in a 2×8 array, as well as associated readout electronics. One such OSMO is shown in Fig. 1. In this section we describe the specifics of the design, including the mechanical features and front-end electronics.

A. Mechanical design

Each scintillator bar is wrapped with at minimum three layers of white Teflon tape. The ends of each bar are coupled to SiPMs using either EJ-560 silicone rubber optical coupling pads [21] or EJ-550 optical grease [22]; we report results for both coupling materials.

The scintillator bars are fed through 3-D printed plastic grids for support and alignment. In order to provide the pressure between the bars and the SiPMs for optimal optical coupling, we use four threaded

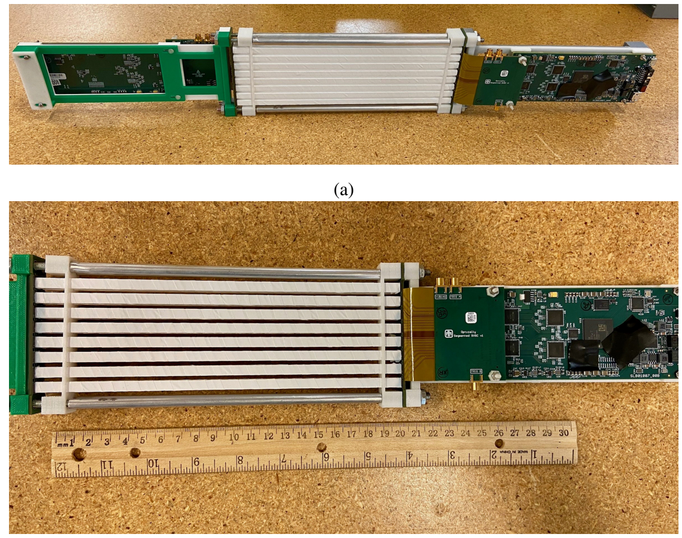

(a)

(b)

Fig. 1: (a) Perspective view of a fully populated optically segmented module (OSMO), with 16 Teflon-wrapped EJ-204 bars. (b) Zoomed in photo of the OSMO for scale, lying flat on the table.

aluminum rods. Screws pass through the plastic guides and a plastic 3-D printed support bracket. This support bracket provides the base for each of the readout boards to be rigidly connected to both the bar support guide and the threaded rods. Finally, two sets of plastic 3-D printed grids ensure that the optical pads and bars are aligned with the SiPMs and provide optical isolation between adjacent channels.

B. Front-end electronics design and data acquisition

A new custom readout system was developed for the OSMO, based closely on a previous design [19]. The electronics components consist of two interconnected PCBs: the SiPM module with a 2×8 SiPM array and the SCEMA waveform capture board.

The SCEMA-B PCB used for all results in this paper is based on the original SCEMA-A design [19], with modifications made to improve FPGA IO mappings, address an existing ADC problem on one channel, and to split functionality to provide a modular front-end. Whereas the SCEMA-A had a front-end that was designed to directly connect to a Planacon MCP-PMT header, the SCEMA-B includes a Samtec connector that allows for implementation of various front-ends, including a similar Planacon interface board, but also allowing for other custom readouts, such as the SiPM module described herein.

The SiPM module, shown in Fig. 2, consists of 16 SensL J-Series SiPMs (MicroFJ-60035-TSV), which have a $6.13\,\mathrm{mm} \times 6.13\,\mathrm{mm}$ cross-section and are separated by $2\,\mathrm{mm}$. A flex section allows two separate rigid PCBs to couple in an orthogonal orientation without an extra connector. The SiPM module is responsible for electrically isolating each of the 16 SiPM anodes in the array.

The SiPM module connects to the SCEMA-B via a SamTec connector (QTH-060-01-L-D-A). On each SCEMA-B are two DRS4 digitizers [23]. Each DRS4 has nine channels: eight of those channels digitize half of the SiPM array and the remaining channel is responsible for digitizing one of the trigger inputs. Thus, the SiPM module routes a total of 18 channels to the SCEMA-B: 16 SiPM channels and 2 trigger channels, which we call Trigger-A and Trigger-B.

The SiPM module also provides MCX connectors for the SiPM bias voltage, which is supplied for these studies by a B&K Precision 9129B DC power supply [24], and for the two trigger channels. Trigger-A can be configured as either an external trigger (received

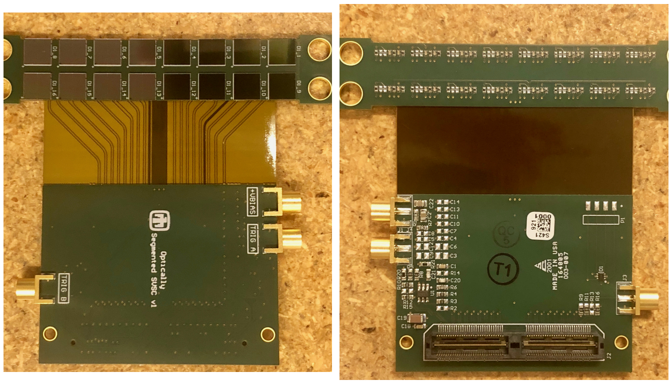

(a) (b)

Fig. 2: The top (a) and bottom (b) sides of the 2×8 OSMO SiPM module board.

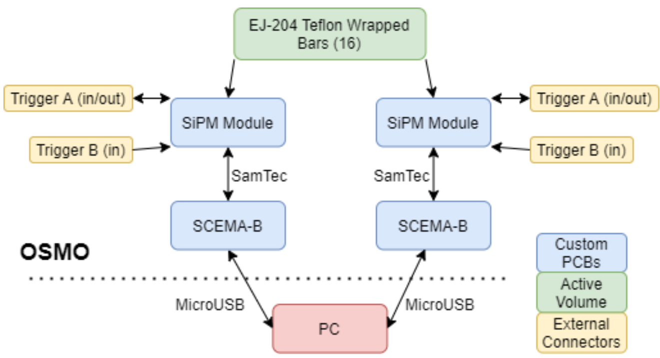

Fig. 3: Diagram of the OSMO DAQ configuration.

via the MCX connector) or as a local sum trigger, depending on whether or not a summing operational amplifier is populated. This sum trigger provides self-triggering capability for one OSMO for acquiring neutron scattering data. The summing circuit reads a common-cathode signal of all 16 SiPMs and routes its output both to a DRS4 channel for digitization and to the Trigger-A MCX connector for output. Trigger-B is configured only as an external trigger; the signal from its MCX connector is simply routed to the SCEMA-B for digitization. Trigger-B is used to input the trace from the tag scintillator for the ^{22}Na calibrations described below, and can also be used to accept a trigger from the other side of the array or from the entire prototype for neutron scatter data.

The OSMO's modular design has at least two different acquisition configurations for the SCEMA-Bs. Each SCEMA-B is able to run independently for module calibrations as well as in a connected state in a multiple OSMO system. This design allows for OSMOs to be assembled and calibrated individually, and then for multiple OSMOs to be connected together to increase the active scintillator volume of a full system. All of the data presented here was collected with each SCEMA-B running independently and with Trigger-A configured as an input trigger. The digitized data were sent from each SCEMA-B to a DAQ computer through a USB-2.0 connection, and are then written to disk. Figure 3 summarizes the DAQ configuration.

III. Module Response Characterization

In this section we describe the full response of a single OSMO, including electrical crosstalk on the SiPM module, SiPM module timing, and scintillator interaction response calibrations for the energy, position, and time. Results are presented for two scintillator/SiPM

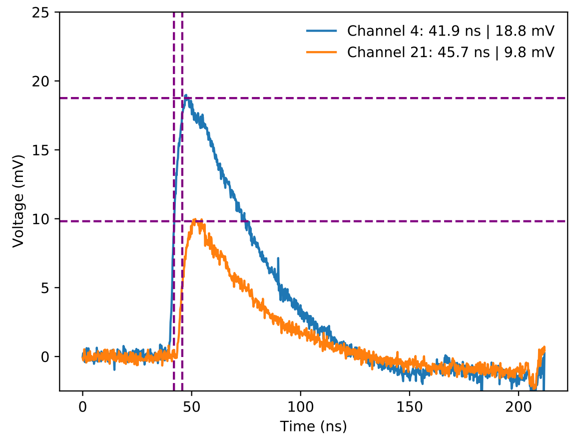

Fig. 4: An example bar interaction from a ^{22}Na source with digitized waveforms for the two SiPMs coupled to the ends of one bar. The vertical lines represent where the analysis identifies the half-point leading-edge of the waveform. The horizontal lines indicate the value the analysis identifies as the pulse height of the waveform.

coupling materials: EJ-550 optical grease and $0.5\,\mathrm{mm}$ thick EJ-560 silicone rubber pads.

A. *Waveform analysis*

Digitized waveforms from the SCEMA-B boards are analyzed with custom C++-based software utilizing ROOT libraries [25]. The values of interest are the leading-edge time of the trigger channels, the leading-edge time of the SiPM traces, and the maximum pulse height for each SiPM waveform. The DRS4s are sampled at $\approx 4.9\,\mathrm{GHz}$, and all 1024 bins within the switched capacitor array (SCA) are digitized for each triggered event. Electrical calibrations for timing and voltage are calculated using a similar procedure to that reported previously [19].

It was also observed that there is some time dependent drift in the voltage calibration for each of the bins within the DRS4 SCA. In order to account for the voltage drift before each run, we subtract from each voltage bin the mean of the voltage of the same bin within the SCA. Before additional processing but after DRS4 electrical calibrations, baseline offsets for the entire waveform are calculated as the mean of the samples 20 through 60 of each waveform. After this procedure we obtain a voltage baseline deviation of $\approx 1.0\,\mu\mathrm{V}$, and voltage noise between $0.3\,\mathrm{mV}$ to $0.5\,\mathrm{mV}$.

Pulse heights of each SiPM trace are measured based on the following algorithm. We first determine the six consecutive samples that give the largest integrated value. We discard the highest and lowest of these six values and report the average of the four remaining values as the pulse height. By dropping the highest and lowest bin voltage values, we avoid noise that appears in some DRS4 bins, which (when present) was always separated by 32 bins and could not be resolved with voltage calibrations alone.

Leading-edge time measurements are determined from the interpolated value between the samples corresponding to $50\,\%$ of the measured pulse height previously discussed. Figure 4 shows the traces from both SiPMs for an example bar interaction. The measured pulse heights and leading-edge times for both traces are indicated by vertical and horizontal dashed lines.

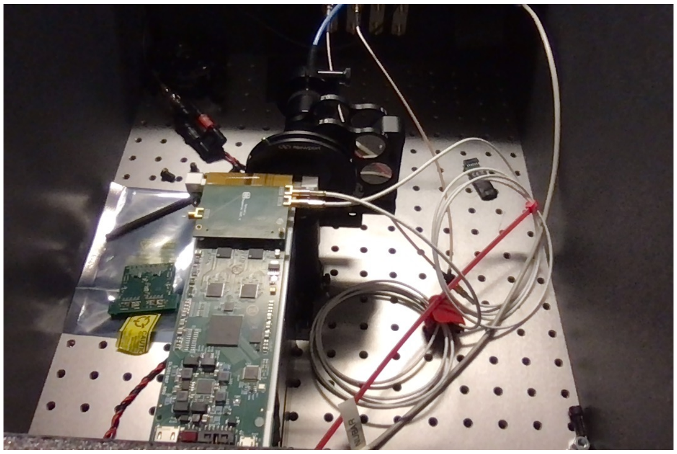

(a)

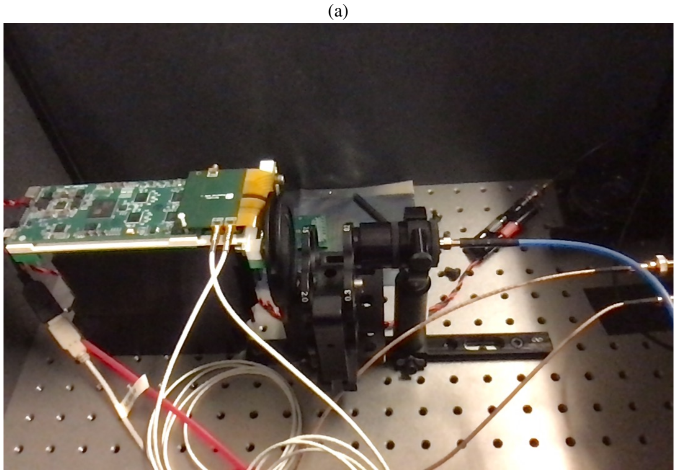

(b)

Fig. 5: (a) Image of the laser setup from behind. The whole SCEMA was aligned to the stationary optical shield to expose a single pixel to the laser. (b) Image of the laser test-setup from the side. The blue cable is an optical fiber which directs the output laser packet. An optical shield and filter are used to isolate a single pixel as the target pixel for the run. The variable optical attenuator was used to tune the SiPM response to the laser.

B. Electrical crosstalk characterization

One motivation for a custom SiPM array was to reduce electrical crosstalk between SiPM channels compared to the commercial J-series array [26] and to the readout chain of the previous OS-SVSC design [11]. To characterize the electrical crosstalk of the system, we used a Photek LPG-405 laser [27] as a known input source on each of the 16 individual SiPM channels, as shown in Fig. 5. The laser was triggered externally using a digital delay and pulse generator from Stanford Research Systems (DG535), which was set to a nominal trigger rate of $50\,\mathrm{Hz}$, approximately the maximum trigger rate for a single SCEMA in this setup. After the DG535 sends a trigger to the laser, the laser then sends a trigger signal to Trigger-B, the independent board trigger, followed $\approx 47\,\mathrm{ns}$ later by an incident photon packet. The resulting waveforms for all channels are then recorded. All electrical crosstalk results are presented with the summing circuit populated.

We measured the amount of electrical crosstalk between a target channel and remaining channels using both the coincident measured pulse height and the total pulse integral of the target channel and the other 15 channels. The pulse height measured for the remaining

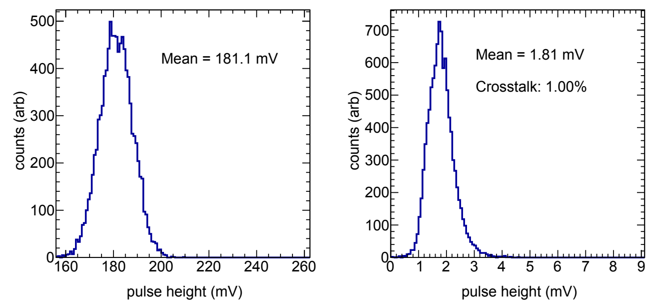

Fig. 6: Example pulse height measurement comparing the distribution of the target channel (left) and an adjacent channel (right).

channels was the measured pulse height using the algorithm defined in Section III-A, where the measured pulse height must happen after $2\,\mathrm{ns}$ before the leading-edge of the target channel's response. This ensures that the appropriate region of interest was measured. Similarly, the waveform integral was calculated for all waveforms beginning $2\,\mathrm{ns}$ before the measured leading-edge of the target channel.

The crosstalk percentage for both the pulse height and the total integral was defined as the mean of each channel's response divided by the mean of the target channel's response. A series of 10k events are recorded when the laser was targeted at a single input pixel. Two example pulse height distributions for one target pixel position are shown in Fig. 6. This procedure was performed using all 16 channels within the array as the target pixel; the results for both the pulse height and the waveform integral are shown in Fig. 7.

The input pixel in Fig. 7 was defined as the target pixel of the laser. Both integral and pulse height measurements are compared as a relative percentage of the input pixel. Target channels 2, 4, 6, 7, 10, 12, 13, and 15 all correspond to one ($1{\times}8$) column within the SiPM module.

We find that the total crosstalk among channels was $\approx$ 1% or less even with relatively large input pulses ($\approx 200\,\mathrm{mV}$) on target channels. Fig. 8 shows the pulse height crosstalk measurement for all channels. The horizontal line is a 0th-order polynomial fit to all data, indicating an average crosstalk of 0.76% for the SiPM module. Since pulse heights used in detector calibration are in the range $15\,\mathrm{mV}$ to $30\,\mathrm{mV}$, a $1\,\%$ crosstalk would imply a pulse height (from only electrical crosstalk) of $150\,\mathrm{\mu V}$ to $300\,\mathrm{\mu V}$. This value is within the measured electrical noise ($\approx 0.5\,\mathrm{mV}$), and we therefore do not expect electrical crosstalk to significantly impact our results. We also note that even after attaching the scintillator bars, we observed similar distributions for the pulse height for non-target channels (as on the right in Fig. 6), and were thus not able to measure any additional optical crosstalk in the populated detector compared to the results shown here.

C. SiPM and readout timing response

In order to validate and understand the reported timing measurements, additional laser studies were performed to characterize the timing resolution as a function of measured pulse height. In order to vary the laser intensity on the SiPM, a variable optical attenuator (shown on right image of Fig. 5) was used. Time measurements are based on the method described in section III-A. Similar to the electrical crosstalk measurements, laser pulses are sent at a rate of $50\,\mathrm{Hz}$ to the SCEMA-B, preceded by a trigger from the DG-535. The time resolution is then defined as the standard deviation from a Gaussian fit to the time difference measured between the arrival time of the input trigger and the leading-edge time of the pulse height.

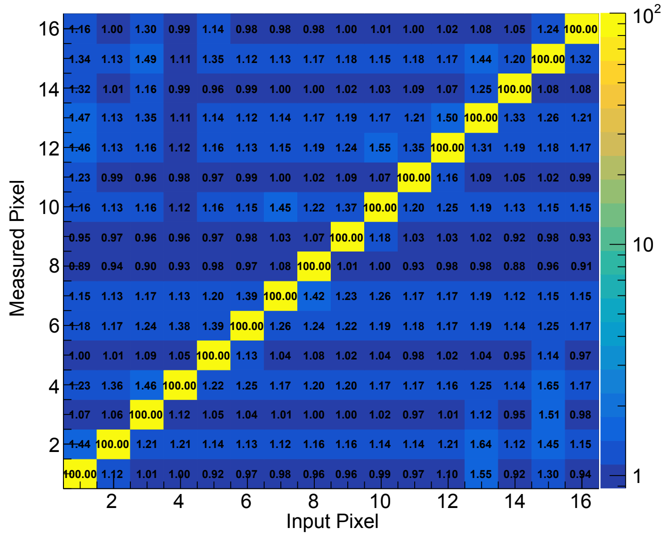

(a)

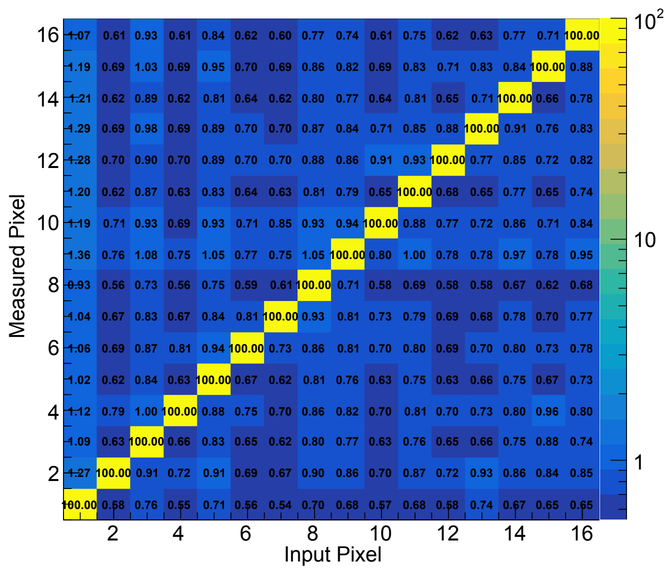

(b)

Fig. 7: (a) Crosstalk integral calculation. (b) Crosstalk pulse height calculation. Results for both graphs are percentages normalized to the input pixel of the laser, where the scale is referenced on the side bars.

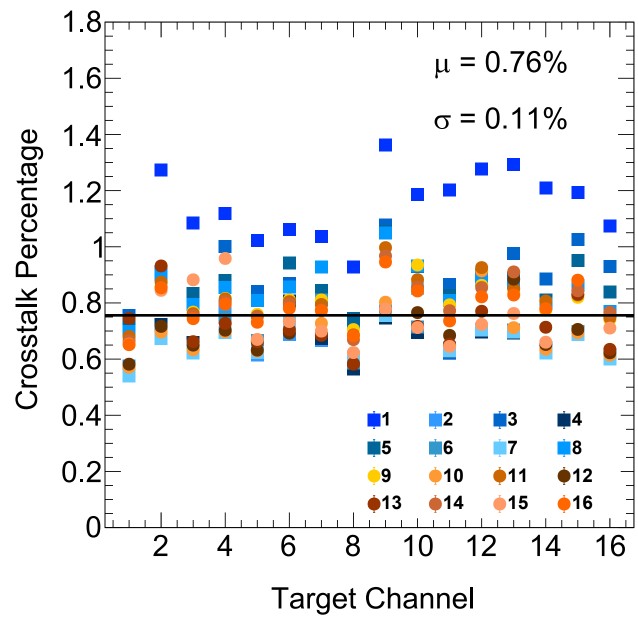

Fig. 8: Distribution of all of the crosstalk in percentages for pulse height. For the zeroth-order fit, we ignore the crosstalk contributions from channel 1, since channel 1 had a known electrical calibration error which skews the results. Statistical error bars are too small to see on the plot.

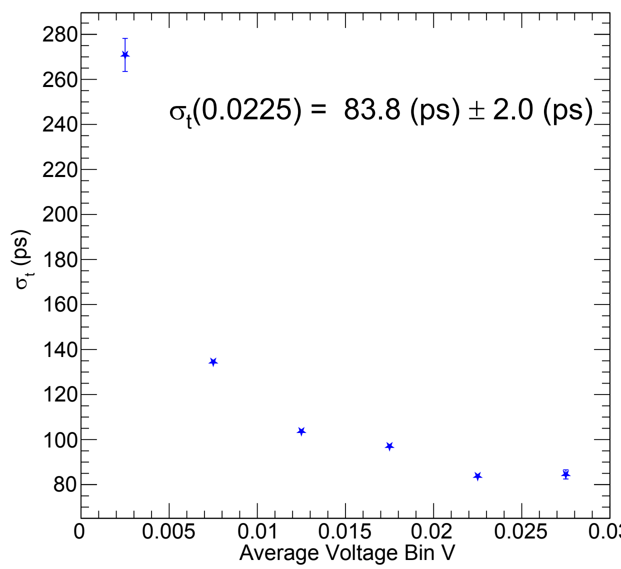

Fig. 9: Example timing resolution of a single SiPM as a function of measured SiPM pulse height. A Photek laser with an optical attenuator is used as an input to a SiPM. The timing resolution is sigma of a Gaussian fit to the difference in time between the trigger and the pulse height. The error bars presented are statistical from the Gaussian fits. The bin range from 20 mV to 25 mV corresponds to the pulse height measured at the ^{22}Na Compton edge ($0.34\,\mathrm{MeV}$).

Figure 9 shows the the approximate timing uncertainty for an example channel as a function of voltage response from the SiPM due to the laser input. Each point represents time differences with pulse height values measured within $2.5\,\mathrm{mV}$ of the plotted point. We find that, as the pulse height increases, the timing resolution improves asymptotically to $\approx 80\,\mathrm{ps}$. Since the reported timing jitter between the laser's trigger and pulse is much less ($T_{sl} = 2\,\mathrm{ps}$ [27]), we find this uncertainty is dominated by the readout electronics, and that the resolution of the timing uncertainty increases as voltage response decreases.

The timing resolution value for small voltages ($< 5\,\mathrm{mV}$, shown as the first point in Fig. 9) is poor compared to the other data points,

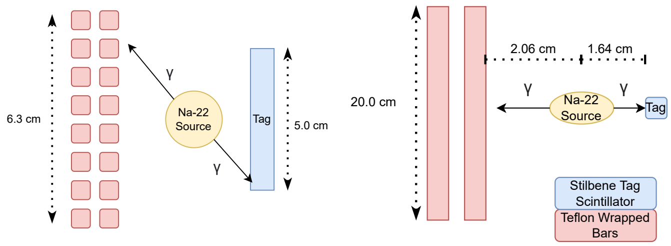

(a) Side view

(b) Top View

Fig. 10: Setup of the ^{22}Na tag scintillator and OSMO.

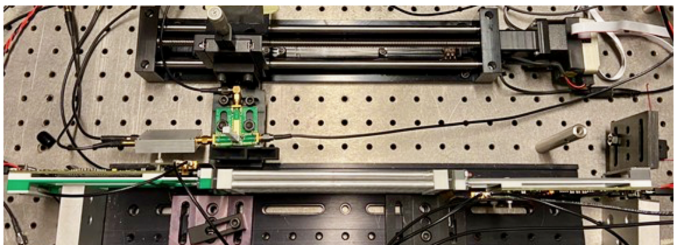

Fig. 11: Top-down view of the ^{22}Na calibration scan procedure is shown. The SensL eval board and tag are on the top of the image, with the ^{22}Na source holder between it and the OSMO.

which indicates that the SiPM's leading-edge time for small pulses is not well measured in the presence of noise. Larger values for the SiPM's voltage response were not measured since pulses greater than $\approx 30\,\mathrm{mV}$ are not used in the calibration procedure described below.

D. Interaction calibration setup

The bar calibration procedure involves a single ^{22}Na source. We use the simultaneous and back-to-back $0.511\,\mathrm{MeV}$ gammas using a procedure similar to methods in both [11] and [15]. The tag scintillator is a teflon-wrapped stilbene crystal that is $5.0\,\mathrm{cm}$ in height and has a $0.5\,\mathrm{cm} \times 0.5\,\mathrm{cm}$ cross section. The tag scintillator rests on top of the J-series SensL eval board SiPM and is optically coupled using EJ-550 optical grease.

Since the crystal's height is approximately $2.0\,\mathrm{cm}$ smaller than total span of the eight scintillator bars, the ^{22}Na source is placed closer ($\approx 1.6\,\mathrm{cm}$) to the tag than to the target bars ($\approx 2.1\,\mathrm{cm}$). This causes a magnification effect so that all of the bars can be targeted by the back-to-back gammas which hit the tag, as shown in Fig. 10. The use of a larger scintillator tag with magnification allows a single scan across the length of the OSMO to target the bars in half of the matrix. In order to precisely move the ^{22}Na source and tag along the length of the OSMO, we use the eTrack $250\,\mathrm{mm}$ linear stage with NEMA 17 MDrive motor from Newmark Systems, which is controlled via the host computer for data acquisition through a USB to RS422 converter. A picture of the experimental setup is shown in Fig. 11.

We comment that the width of the tag scintillator ($0.5\,\mathrm{cm}$) introduces a contribution to the width of the reconstructed z-position measurement. If we assume that gammas are uniformly distributed over the width of the tag and we account for the magnification (M $\approx$ 2.1 / 1.6) between the tag and target bars we find this contribution to be: $\sigma_{z-tag} = M \cdot 0.5/\sqrt{12} \approx 0.2\,\mathrm{cm}$, which is about an order of magnitude less than reported results in Section IV, Tables I and II.

The two independent SCEMA-B boards are powered by a B&K Precision 9129B DC power supply, which provides two independent channels of $5.6\,\mathrm{VDC}$ power, and are connected to a control computer via micro-USB through a USB hub. The SiPMs are provided a $30\,\mathrm{V}$ bias, or an approximate $6\,\mathrm{V}$ over-voltage, supplied by a B&K Precision 1761 power supply. Additionally, $30\,\mathrm{VDC}$ is supplied to a single SensL J-series eval board which is used to read out the tag scintillator. We use both the standard and fast outputs from the eval board. The standard output is sent to a Photek PA200-10 (Mini-Circuits ZFL-1000LN+) $20\,\mathrm{dB}$ amplifier, which is routed to the DG535 pulse generator as the system trigger.

We now provide a brief description of the readout procedure. For an input trigger, we set a $0.18\,\mathrm{V}$ threshold on the DG535. When the threshold on the DG535 is exceeded, the DG535 then issues two parallel triggers ($200\,\mathrm{mV}$ step function) with $5\,\mathrm{ps}$ jitter [28] to the input Trigger-A of each SCEMA-B. After the SCEMA-Bs receive a trigger, the fast output from the tag scintillator is recorded on the Trigger-B of one SCEMA-B, along with all other SiPM waveforms. This allows the system to digitize the fast-output spectrum from the tag and thus measure both a reference time for the interaction and the tag's ^{22}Na pulse height spectrum.

E. Interaction energy response

The energy spectrum for each bar was fit in the range of $0.225\,\mathrm{MeV}$ to $0.4\,\mathrm{MeV}$ to the predicted Klein-Nishina spectrum for back-to-back $0.511\,\mathrm{MeV}$ gammas using the method described in [15]. This energy calibration was performed for the two photodetectors coupled to the ends of each bar; an example is shown in Fig. 12. The resulting scaling factors for each of the photodetectors were used to convert measured pulse height in mV to an energy in MeVee.

In the following sections we present the position and time resolution of the bars for events within different energy ranges and fit the results to a power law. We quote the position and time resolution energy ranges from $0.0\,\mathrm{MeVee}$ to $0.4\,\mathrm{MeVee}$ in steps of $0.10\,\mathrm{MeVee}$, which fully covers the Compton spectrum resulting from $0.511\,\mathrm{MeVee}$ gammas from the ^{22}Na source.

F. Interaction position resolution

The interaction position along a bar is determined by measuring both the difference in leading-edge times and the log of the ratio of the measured pulse heights in the two SiPMs. In order to obtain an overall position resolution we combine the reconstructed positions from both amplitude and time measurements. The method we use to combine these two measurements relies on the variance and covariance of the two measurements, and is known as the Best Linear Unbiased Estimator (BLUE), which is further described in [29], and a short description is given below.

Given two results $\theta = \hat{\theta}_1 \pm \sigma_1$ and $\theta = \hat{\theta}_2 \pm \sigma_2$, the BLUE is

$$\hat{\theta} = \frac{\hat{\theta}_1(\sigma_2^2 - \rho\sigma_1\sigma_2) + \hat{\theta}_2(\sigma_1^2 - \rho\sigma_1\sigma_2)}{\sigma_1^2 - 2\rho\sigma_1\sigma_2 + \sigma_2^2}\,, \tag{3}$$

with variance

$$\sigma_{\hat{\theta}}^2 = \frac{\sigma_1^2\sigma_2^2(1-\rho^2)}{\sigma_1^2 - 2\rho\sigma_1\sigma_2 + \sigma_2^2}\,, \tag{4}$$

where ρ is the correlation between uncertainties [29]. For the combined measurements below, we treat the uncertainties as uncorrelated.

The interaction position using SiPM pulse heights from each bar is determined by the log of the amplitude ratio (LAR) between the two bar ends, or $\ln\frac{A_1}{A_2}$, where A_1 and A_2 are the pulse heights measured from the output SiPMs from the end of each bar. The mean LAR as a function of interaction position for Bar 1 in the $0.3\,\mathrm{MeVee}$ to $0.4\,\mathrm{MeVee}$ range, measured with a Gaussian fit to the distribution, is shown in Fig. 13a. The standard deviation of the distribution as a function of interaction position is shown in Fig. 13b. The reported position resolution for this bar, which was coupled with

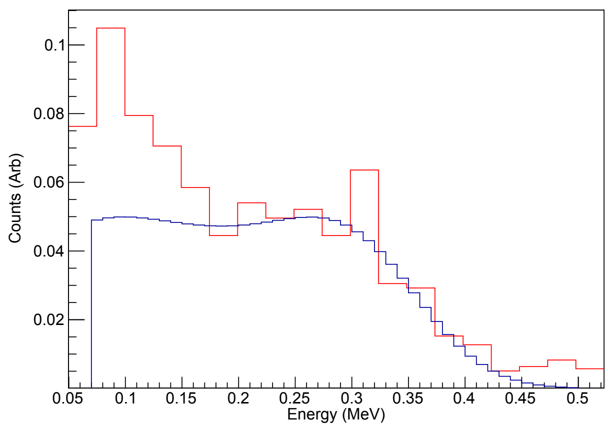

(a)

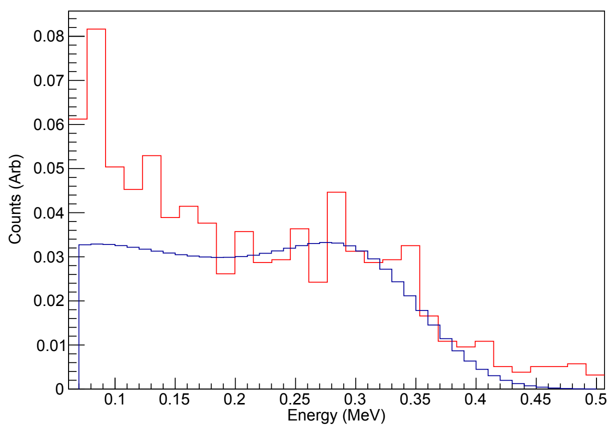

(b)

Fig. 12: Example of an energy calibration for a single bar. The red and blue histograms represent data and the fit respectively. The region of interest for the Klein-Nishina fit is $0.225\,\mathrm{MeVee}$ to $0.4\,\mathrm{MeVee}$. (a)/(b) Shows the fit to the Klein-Nishina prediction for the two photodetectors on each bar end.

optical grease to the SiPM, is the average LAR width divided by the slope of the LAR means, or $1.8\,\mathrm{cm}$. Fig. 14 shows the LAR as a function of interaction position for all 16 bars coupled with optical grease coupling.

In previous studies [11, 15], the position resolution using timing was computed by taking the difference of the pulse leading-edge time for each SiPM from the end of each bar: $t_1 - t_2$. However, in this case the time measurements on a single OSMO are measured using two different SCEMA-Bs. In these measurements, the two SCEMA-Bs and their corresponding DRS4s run asynchronously. We therefore use the time of the synchronized trigger pulse from the DG-535 into the Trigger-A inputs ($T_{1,2}^A$) in order to align the timing between SCEMAs:

$$\Delta t = (T_1^A - t_1) - (T_2^A - t_2). \tag{5}$$

From the above equation, we substitute $T_i = T_i^A - t_i$ to identify the relative time difference measured on each SCEMA and obtain equation:

$$\Delta t = T_1 - T_2. \tag{6}$$

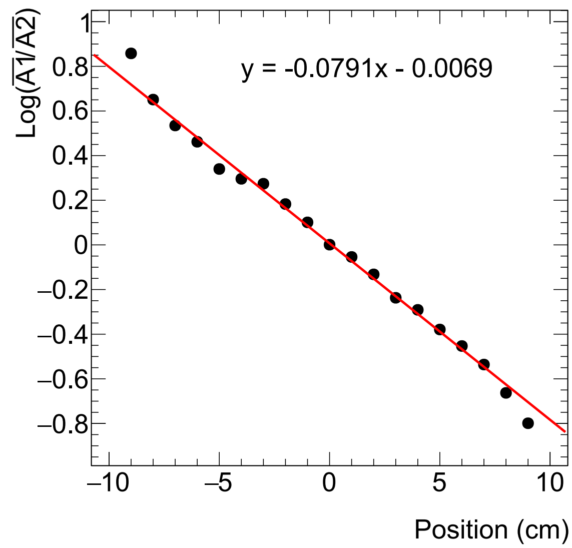

(a)

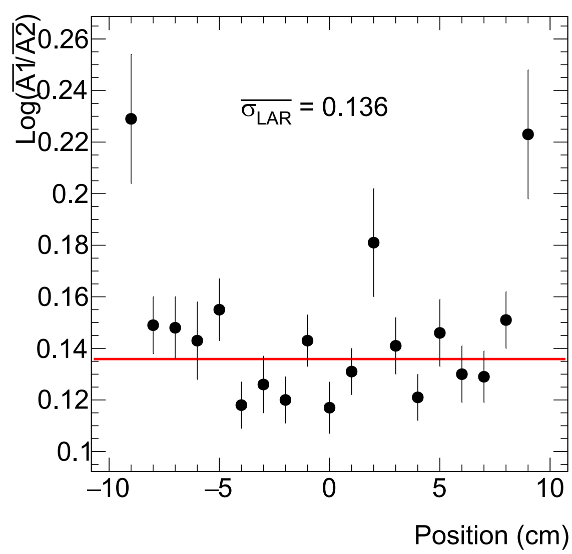

(b)

Fig. 13: Example dependence of the mean LAR as a function of source position for Bar 1 in the OSMO. After energy calibrations to determine the MeVee/mV ratio for each bar, a cut is performed to filter only events in the $0.3\,\mathrm{MeVee}$ to $0.4\,\mathrm{MeVee}$ range. Then the LAR is calculated and a Gaussian fit is performed for each source position. Data points and uncertainties in (a) are the Gaussian mean and uncertainties reported from the (ROOT default) fitting algorithm. In (a), error bars are smaller than the markers. Data points and uncertainties in (b) are the fitted Gaussian sigma and the uncertainties reported from the fitting algorithm.

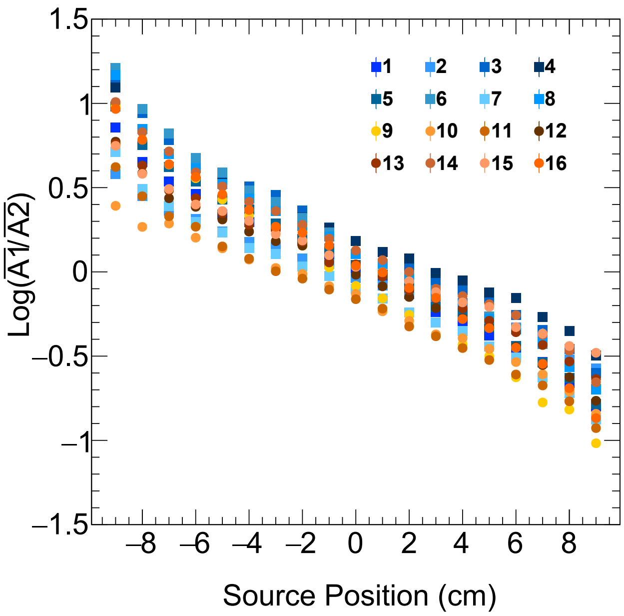

Fig. 14: The mean LAR for all of the bars as a function of the interaction position.

Figure 15 shows the mean and standard deviation of the time difference distributions as function of interaction position for Bar 1 coupled with optical grease, again in the 0.3 MeVee to 0.4 MeVee range. The position resolution using time difference for this bar is 2.08 cm. Fig. 16 shows the mean of time difference for all 16 bars with optical grease coupling: the two different y-intercept distributions correspond to the two different DRS4 pairs on each SCEMA-B, resulting in distinct timing offsets. The bottom 8 bars correspond to when a bar's SiPM channels are read by the same DRS4 as the trigger channel, and the top 8 bars' SiPM channels are digitized by the other DRS4. The combined BLUE position resolution as a function of energy is shown in Fig. 17, in which the mean position resolution for all 16 bars is used.

G. Interaction time response

In addition to reconstructing the z-position of an event, an OS-SVSC also needs to be able to reconstruct a scatter's event time as well as time order multiple scatters within a single event. This is the purpose of the definition of the interaction time. The interaction time, T_{int}, is defined as the average of the leading-edge times for each SiPM end minus the leading-edge time of the large-tag scintillator (t_1^B), which is used as a time reference. As before, the leading-edge time of each bar end has a correction from the Trigger-A input to correct for the asynchronous SCEMA acquisition, including the tag's leading-edge time input to Trigger-B. Therefore, the equation for the interaction time becomes:

$$T_{int} = \frac{(T_1^A - t_1) + (T_2^A - t_2)}{2} - (T_1^A - t_1^B). \quad (7)$$

The mean and standard deviation of the interaction time distributions as a function of interaction position for Bar 1 coupled with optical grease are shown in Fig. 18: the reported interaction resolution is 222 ps for this bar. It has been previously observed that interaction time within a bar has a positional dependence along a bar's length [15], which is again observed here. The energy-dependent average interaction time resolution is shown in Fig. 19. The offset

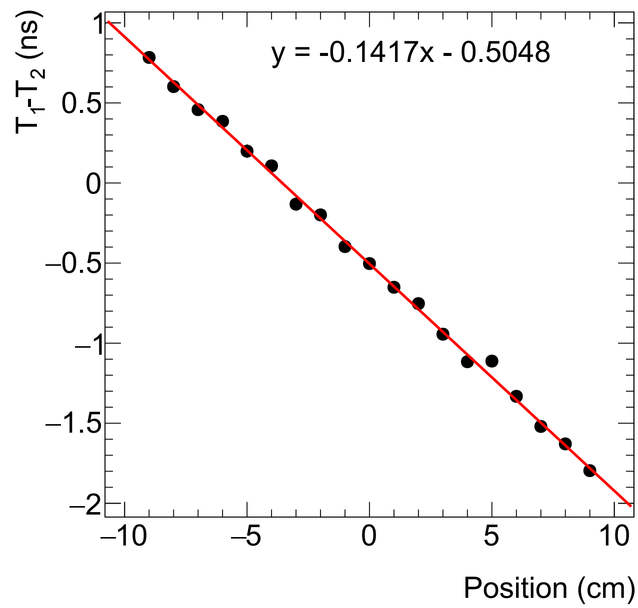

(a)

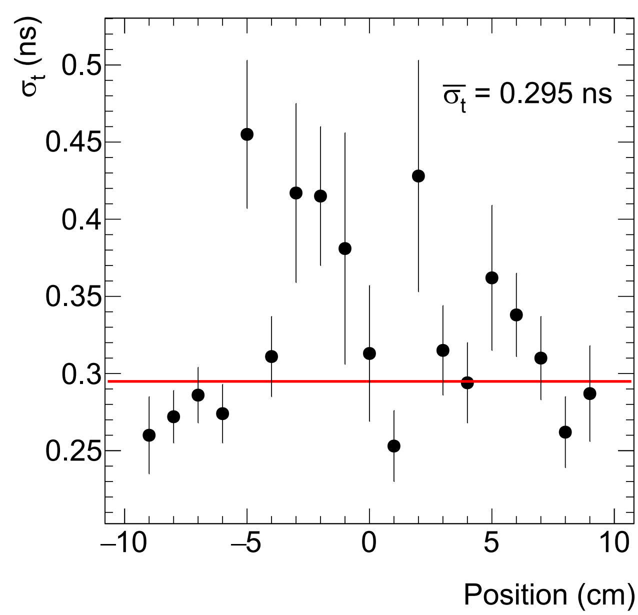

(b)

Fig. 15: Example dependence of the time difference as a function of source position for Bar 1 in the OSMO. After energy calibrations to determine the MeVee/mV ratio for each bar, a cut is performed to filter only events in the 0.3 MeVee to 0.4 MeVee range. Then the time difference is calculated and a Gaussian fit is performed for each source position. Data points and uncertainties in (a) are the Gaussian mean and uncertainties reported from the (ROOT default) fitting algorithm. In (a), error bars are smaller than the markers. Data points and uncertainties in (b) are the fitted Gaussian sigma and the uncertainties reported from the fitting algorithm.

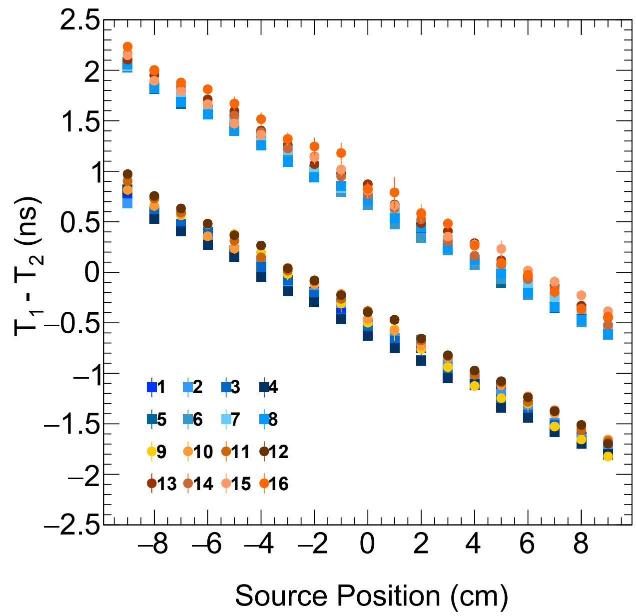

Fig. 16: The results of a Gaussian fit to the time difference for all bars at different ^{22}Na scan positions. The points represent the means and the error bars are the sigma from the fit. The two different y-intercept distributions correspond to bars digitized by the same DRS4 as the trigger channel (bottom group) and other DRS4 (top group), and represent the timing offset between the two DRS4s.

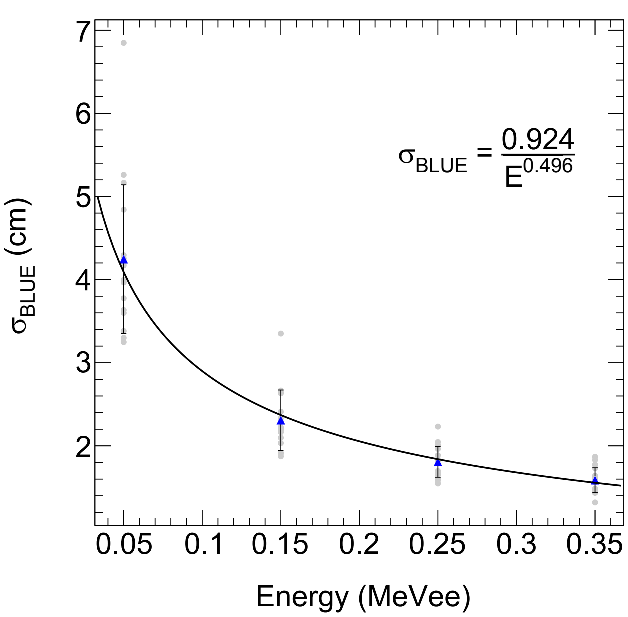

Fig. 17: The average position resolution for each bar as a function of energy is fit to a power law. Each point's value along the x-axis represents the mean value of the range. The grey points indicate the results for the 16 bars in the OSMO. The blue points indicate the mean of the 16 bars. The error bars on the mean data points represent the standard deviation of the mean of the 16 bars. The fit is then applied to the blue points.

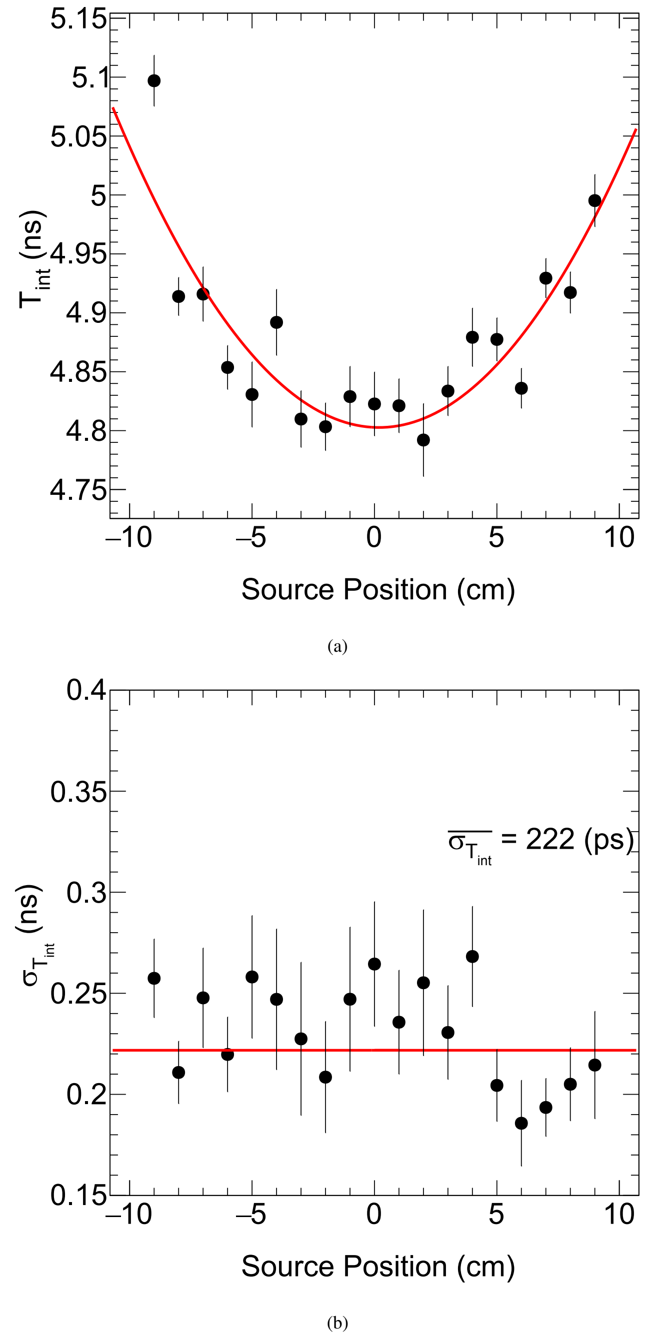

Fig. 18: (a) Interaction time is shown for an example bar (Bar1), in the module. We expect a symmetrical effect about the bar length, for any given positional dependence of the interaction time. (b) The average uncertainty in the interaction time for Bar 1 at each of the scan positions. We fit a zeroth order polynomial to find an average uncertainty for each bar.

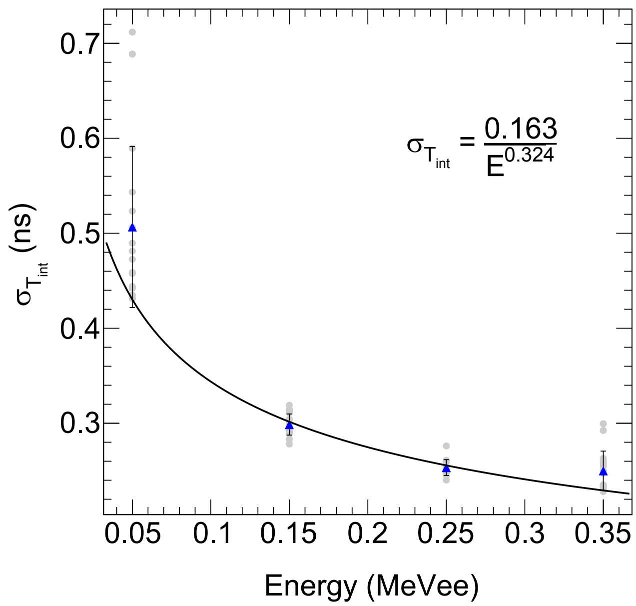

Fig. 19: The average interaction time for each bar is fit to a power law. The grey points indicate the results for the 16 bars in the OSMO. The blue points indicate the mean of the 16 bars. The error bars on the mean data points represent the standard deviation of the mean of the 16 bars. The fit is then applied to the blue points.

from the interaction time in Fig. 18 occurs from the minimum average delay time from equation (7).

Finally, we conclude this section by commenting on the contribution to the interaction uncertainty due to the large-tag trigger, $T_1^A - t_1^B$. If we assume that the uncertainties for all measured times are uncorrelated, and after accounting for measured uncertainties in leading-edge times of the SiPMs, the remaining uncertainty introduced by the large-tag trigger ($T_1^A - t_1^B$) would be $\approx 80\,\mathrm{ps}$, which we estimate as the timing uncertainty introduced by the electrical readout (described in section III-C), plus the contribution introduced by the large-tag scintillator. However, the correlations between the different times (T_1^A, T_2^A, t_2, t_1 and t_1^B) are not measured, therefore the exact propogation of uncertainty for the interaction time in equation (7) is not possible.

IV. Summary of results and discussion

Here we present position and interaction time resolution results for all 16 channels in the assembled OSMO. Tables I and II summarize the position and timing resolutions for EJ-550 and EJ-560 optical coupling material, respectively. In the last two rows, we report the mean and standard deviation of the given resolution across the 16 bars. The values in the columns are (in order) the bar number, the z-positon reconstructed with time, amplitude, combined (BLUE), and finally the interaction time resolution.

We note that overall, the EJ-550 optical coupling has improved position and timing resolution values compared to EJ-560. However, there are some bars for which the EJ-560 silicone pads have better position resolution than with optical grease. Compared to the EJ-550 data, resolution values are noticeably better for bars 2, 7, and 15. All three of these bars are also close to the tightening screws on the OSMO. One possibility is that these bars have better optical coupling between the scintillator and SiPM in the optical pad configuration due to better compression or alignment, and therefore the SiPMs collected

TABLE I: Z-position resolution (using timing, amplitude, and BLUE) and interaction time resolution results with EJ-550 optical grease coupling for all 16 bars.

Bar ID	σ_z^t (cm)	σ_z^A (cm)	σ_z^{BLUE} (cm)	σ_{int} (ps)
1	2.08	1.72	1.34	222
2	2.44	2.76	1.83	244
3	1.94	1.71	1.29	242
4	1.95	2.11	1.43	233
5	1.91	1.79	1.31	226
6	1.93	1.65	1.26	227
7	2.22	2.16	1.55	228
8	2.06	1.85	1.38	231
9	1.78	1.52	1.16	234
10	2.32	2.68	1.76	247
11	2.06	2.07	1.46	229
12	1.99	2.13	1.46	239
13	2.13	2.16	1.52	224
14	2.18	1.95	1.46	238
15	2.53	2.54	1.79	263
16	1.98	1.56	1.24	240
$\bar{x}$	2.09	2.02	1.45	235
σ_{std}	0.20	0.37	0.19	10

TABLE II: Z-position resolution (using timing, amplitude, and BLUE) and interaction time resolution results with EJ-560 silicone pads for coupling for all 16 bars.

Bar ID	σ_z^t (cm)	σ_z^A (cm)	σ_z^{BLUE} (cm)	σ_{int} (ps)
1	2.41	2.19	1.62	253
2	2.13	2.42	1.61	244
3	3.00	4.81	2.70	258
4	2.83	4.33	2.48	264
5	2.99	4.95	2.73	262
6	2.60	3.55	2.15	297
7	2.04	1.76	1.34	238
8	2.02	1.88	1.38	248
9	2.29	2.20	1.59	263
10	7.45	9.28	5.90	352
11	2.82	3.16	2.11	264
12	3.53	6.47	3.41	300
13	3.04	2.49	1.95	280
14	2.75	2.57	1.88	250
15	2.16	1.96	1.45	237
16	2.18	2.05	1.50	236
$\bar{x}$	2.89	3.50	2.24	265
σ_{std}	1.25	1.99	1.10	29

more light. Figure 20 highlights the differences in position resolution between the two optical-coupling configurations.

We observe the average and standard deviation of position resolution for the 16 bars coupled with EJ-550 to be $1.45\,\mathrm{cm} \pm 0.19\,\mathrm{cm}$ and with EJ-560 to be $2.24\,\mathrm{cm} \pm 1.10\,\mathrm{cm}$. We also observe an average and standard deviation of the interaction time resolution for the 16 bars with EJ-550 to be $235\,\mathrm{ps} \pm 10\,\mathrm{ps}$ and with EJ-560 to be $265\,\mathrm{ps} \pm 29\,\mathrm{ps}$. We note that bar number 10 had substantially different position resolution with the EJ-560 coupling, which we also attribute to poor light collection of the optical pad.

One source of the difference in overall position and interaction time resolutions between the two configurations is the amount of light collected at the ends of the SiPMs. Figure 21 highlights the differences in the results of the energy calibrations for each of the photodetectors for each bar. The energy calibration results show the amplitude response (in mV) calculated for the Compton edge of the ^{22}Na source. A decreased amplitude response corresponds to an overall decrease in the light collected by the SiPM. A decrease in the amplitude response from a SiPM directly affects both the timing resolution by affecting SiPM's response time (Fig. 9) and amplitude

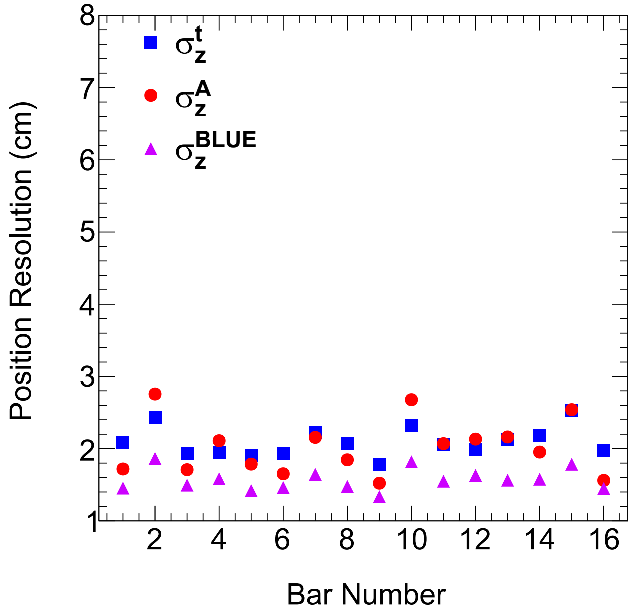

(a) EJ-550 optical grease

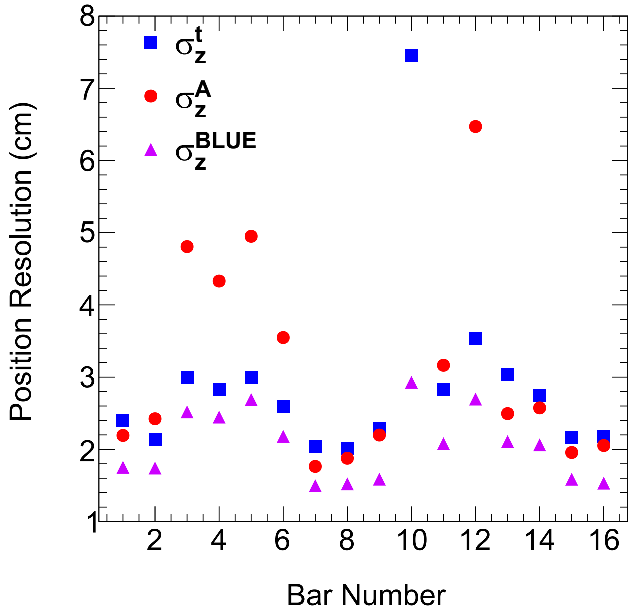

(b) EJ-560 silicone pads

Fig. 20: (a) A graphical representation of Table I. (b) A graphical representation of Table II. The amplitude resolution for Bar 10 does not fit into the scale shown.

resolution by reducing the signal-to-noise ratio of the measured pulse. Therefore, a decrease in the amount of light collected (a lower amplitude response) will negatively affect both interaction time and position reconstruction.

We highlight the light collection difference by noticing that bars 1, 2, 7, 8, 9, 15, 16 from EJ-560 have approximately the same light collection as the EJ-550 (Figure 21). We compare only this subset for the overall for the combined z-position reconstruction and interaction time. In this subset, we find EJ-550 has a combined z-position resolution result of $1.47\,\mathrm{cm} \pm 0.24\,\mathrm{cm}$ compared with the EJ-560 $1.50\,\mathrm{cm} \pm 0.10\,\mathrm{cm}$. The interaction time measurement with

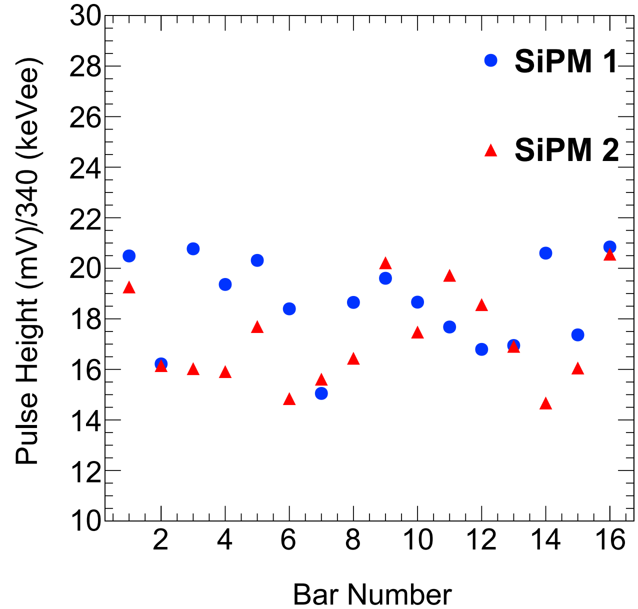

(a) EJ-550 optical grease

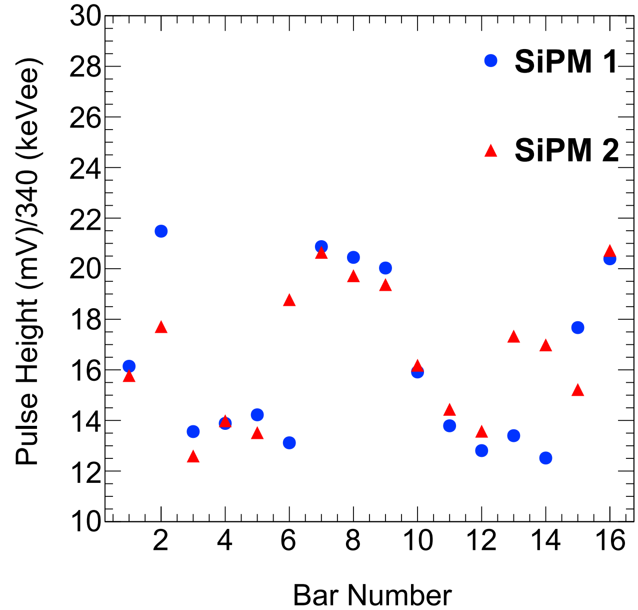

(b) EJ-560 silicone pads

Fig. 21: (a) Pulse height response in mV to a $340\,\mathrm{keVee}$ gamma interaction using the EJ-550 optical grease dataset. (b) Pulse height response in mV to a $340\,\mathrm{keVee}$ gamma interaction using the EJ-560 silicone pad dataset.

EJ-550 has an uncertainty of $237\,\mathrm{ps} \pm 12\,\mathrm{ps}$ compared with the EJ-560 $245\,\mathrm{ps} \pm 9\,\mathrm{ps}$. Therefore, we conclude that the overall drop in resolution when using EJ-560 was due to the lower average light collection in the full set of bars.

Another source of timing uncertainty is the use of multiple DRS4s which share independent clocks between the two unsynchronized SCEMA-Bs. Previous studies [15] relied on digitization chains that used channels all on a single synchronized DRS4. We observe that the first OS prototype [11], which also used asynchronous readouts for the two SiPMs and used similar scintillators, reported a poorer timing-based position resolution compared to amplitude reconstruction ($3.5\,\mathrm{cm}$ compared to $1\,\mathrm{cm}$ at $1\,\mathrm{MeV}$). We also note that one other potential source of additional timing uncertainty may be the use of $20\,\mathrm{cm}$ long EJ-204 scintillator bars in this study compared to $19\,\mathrm{cm}$ as in previous studies.

Compared to previous results based on single bar measurements [15], we observe an increase in combined position reconstruction uncertainty from $\approx 1.0\,\mathrm{cm}$ to $\approx 1.45\,\mathrm{cm}$. Additionally, we observe that the interaction time uncertainty has increased from $154\,\mathrm{ps} \pm 3\,\mathrm{ps}$ to $235\,\mathrm{ps} \pm 10\,\mathrm{ps}$. Position reconstruction and interaction time resolution could be improved both with increased light detected by a SiPM and in an OSMO where both SCEMAs are controlled synchronously, which allows all DRS4s to operate with a common clock. Synchronized SCEMA-Bs would eliminate the need to measure $T^A_{1,2}$ and remove the substitution required in (5) and (7).

V. Conclusions

We have designed, assembled, and characterized a modular SiPM-based scintillator array as a base unit for a high-efficiency and portable double scatter neutron imaging system. We have compared detector calibration results for a single module using both EJ-560 and EJ-550 as optical couplings.

We find that, on average, EJ-550 optical grease outperforms the EJ-560 silicone pads, which we attribute to improved light collection by each SiPM due to improved optical coupling. We therefore find that a major factor affecting an OSMO's position reconstruction and interaction time resolutions are the variable optical couplings among the 16 bars. Since the optical coupling affects the amount of light collected by the SiPM, it also affects the SiPM's timing response which directly affects both the interaction time uncertainty and the position reconstruction uncertainty.

We find that improved interaction time resolutions and position reconstruction would result both from better optical coupling and with synchronized SCEMA-Bs. Finally, we note that SiPM electronic readout and scintillator differences relative to [15] may have also contributed to the differences in both measured position reconstruction and interaction time resolutions. Plans for future work include calibrating additional OSMOs, and to combine multiple-synchronized OSMOs together into a fully realized neutron imaging system. Current neutron-imaging tests are being performed using the single calibrated module presented here with the EJ-550 optical grease for coupling.

Acknowledgment

Sandia National Laboratories is a multimission laboratory managed and operated by National Technology and Engineering Solutions of Sandia, LLC, a wholly owned subsidiary of Honeywell International, Inc., for the U.S. Department of Energy's National Nuclear Security Administration under contract DE-NA0003525. This paper describes objective technical results and analysis. Any subjective views or opinions that might be expressed in the paper do not necessarily represent the views of the U.S. Department of Energy or the United States Government. This document is approved for relase under release number SAND2021-15772 O.

References

[1] J. Manfredi, E. Adamek, J. A. Brown, E. Brubaker, B. Cabrera-Palmer, J. W. Cates, R. Dorrill, A. Druetzler, J. Elam, P. L. Feng, M. Folsom, A. Galindo-Tellez, B. L. Goldblum, P. Hausladen, N. Kaneshige, K. Keefe, T. A. Laplace, J. Learned, A. Mane, P. Marleau, J. Mattingly, M. Mishra, A. Moustafa, J. Nattress, K. Nishimura, J. Steele, M. Sweany, K. Weinfurther, K.-P. Ziock, The single-volume scatter camera, in: M. Fiederle, A. Burger, S. A. Payne (Eds.), Hard X-Ray, Gamma-Ray, and Neutron Detector Physics XXII, SPIE, 2020, p. 114940V. doi:10.1117/12.2569995.
URL https://doi.org/10.1117/12.2569995

[2] W. C. Sailor, R. C. Byrd, A. Gavron, R. Hammock, Y. Yariv, A neutron source imaging detector for nuclear arms treaty verification, Nuclear Science and Engineering 109 (3) (1991) 267–277. doi:10.13182/nse91-a23852.
URL https://doi.org/10.13182/nse91-a23852

[3] N. Mascarenhas, J. Brennan, K. Krenz, P. Marleau, S. Mrowka, Results with the neutron scatter camera, IEEE Transactions on Nuclear Science 56 (3) (2009) 1269–1273. doi:10.1109/tns.2009.2016659.
URL https://doi.org/10.1109/tns.2009.2016659

[4] A. C. Madden, P. F. Bloser, D. Fourguette, L. Larocque, J. S. Legere, M. Lewis, M. L. McConnell, M. Rousseau, J. M. Ryan, An imaging neutron/gamma-ray spectrometer, in: A. W. Fountain (Ed.), Chemical, Biological, Radiological, Nuclear, and Explosives (CBRNE) Sensing XIV, SPIE, 2013, p. 87101L. doi:10.1117/12.2018075.
URL https://doi.org/10.1117/12.2018075

[5] J. E. M. Goldsmith, M. D. Gerling, J. S. Brennan, A compact neutron scatter camera for field deployment, Review of Scientific Instruments 87 (8) (2016) 083307. doi:10.1063/1.4961111.
URL https://doi.org/10.1063/1.4961111

[6] A. Poitrasson-Rivière, M. C. Hamel, J. K. Polack, M. Flaska, S. D. Clarke, S. A. Pozzi, Dual-particle imaging system based on simultaneous detection of photon and neutron collision events, Nuclear Instruments and Methods in Physics Research Section A: Accelerators, Spectrometers, Detectors and Associated Equipment 760 (2014) 40–45. doi:10.1016/j.nima.2014.05.056.
URL https://doi.org/10.1016/j.nima.2014.05.056

[7] J. Braverman, J. Brennan, E. Brubaker, B. Cabrera-Palmer, S. Czyz, P. Marleau, J. Mattingly, A. Nowack, J. Steele, M. Sweany, K. Weinfurther, E. Woods, Single-volume neutron scatter camera for high-efficiency neutron imaging and spectroscopy, arXiv:1802.05261, https://arxiv.org/abs/1802.05261 (Feb. 2018).

[8] T. Laplace, B. Goldblum, J. Brown, D. Bleuel, C. Brand, G. Gabella, T. Jordan, C. Moore, N. Munshi, Z. Sweger, A. Sweet, E. Brubaker, Low energy light yield of fast plastic scintillators, Nuclear Instruments and Methods in Physics Research Section A: Accelerators, Spectrometers, Detectors and Associated Equipment 954 (2020) 161444. doi:10.1016/j.nima.2018.10.122.
URL https://doi.org/10.1016/j.nima.2018.10.122

[9] G. R. Jocher, J. Koblanski, V. A. Li, S. Negrashov, R. C. Dorrill, K. Nishimura, M. Sakai, J. G. Learned, S. Usman, miniTimeCube as a neutron scatter camera, AIP Advances 9 (3) (2019) 035301. doi:10.1063/1.5079429.
URL https://doi.org/10.1063/1.5079429

[10] K. Weinfurther, J. Mattingly, E. Brubaker, J. Steele, Model-based design evaluation of a compact, high-efficiency neutron scatter camera, Nuclear Instruments and Methods in Physics Research Section A: Accelerators, Spectrometers, Detectors and Associated Equipment 883 (2018) 115–135. doi:10.1016/j.nima.2017.11.025.
URL https://doi.org/10.1016/j.nima.2017.11.025

[11] A. Galindo-Tellez, K. Keefe, E. Adamek, E. Brubaker, B. Crow, R. Dorrill, A. Druetzler, C. Felix, N. Kaneshige, J. Learned, J. Manfredi, K. Nishimura, B. P. Souza, D. Schoen, M. Sweany, Design and calibration of an optically segmented single volume scatter camera for neutron imaging, Journal of Instrumentation 16 (04) (2021) P04013. doi:10.1088/1748-0221/16/04/p04013.
URL https://doi.org/10.1088/1748-0221/16/04/p04013

[12] W. M. Steinberger, M. L. Ruch, N. Giha, A. D. Fulvio, P. Marleau, S. D. Clarke, S. A. Pozzi, Imaging special nuclear material using a handheld dual particle imager, Scientific Reports 10 (1) (Feb. 2020). doi:10.1038/s41598-020-58857-z.
URL https://doi.org/10.1038/s41598-020-58857-z

[13] M. Wonders, M. Flaska, Application of an added-sinusoid, signal-multiplexing scheme to a compact, multiplexed neutron scatter camera, Nuclear Instruments and Methods in Physics Research Section A: Accelerators, Spectrometers, Detectors and Associated Equipment 1002 (2021) 165294. doi:10.1016/j.nima.2021.165294.
URL https://doi.org/10.1016/j.nima.2021.165294

[14] X. Pang, Z. Zhang, J. Zhang, W. Zhou, Y. Zhang, D. Cao, L. Shuai, Y. Wang, Y. Liu, X. Jiang, X. Liang, X. Xiao, L. Wei, D. Li, A compact MPPC-based camera for omnidirectional (4π) fast-neutron imaging based on double neutron–proton elastic scattering, Nuclear Instruments and Methods in Physics Research Section A: Accelerators, Spectrometers, Detectors and Associated Equipment 944 (2019) 162471. doi:10.1016/j.nima.2019.162471.
URL https://doi.org/10.1016/j.nima.2019.162471

[15] M. Sweany, A. Galindo-Tellez, J. Brown, E. Brubaker, R. Dorrill, A. Druetzler, N. Kaneshige, J. Learned, K. Nishimura, W. Bae, Interaction position, time, and energy resolution in organic scintillator bars with dual-ended readout, Nuclear Instruments and Methods in Physics Research Section A: Accelerators, Spectrometers, Detectors and Associated Equipment 927 (2019) 451–462. doi:10.1016/j.nima.2019.02.063.
URL https://doi.org/10.1016/j.nima.2019.02.063

[16] W. Steinberger, M. Ruch, A. Di-Fulvio, S. Clarke, S. Pozzi, Timing performance of organic scintillators coupled to silicon photomultipliers, Nuclear Instruments and Methods in Physics Research Section A: Accelerators, Spectrometers, Detectors and Associated Equipment 922 (2019) 185–192. doi:10.1016/j.nima.2018.11.099.
URL https://doi.org/10.1016/j.nima.2018.11.099

[17] S. Surti, J. S. Karp, Update on latest advances in time-of-flight pet, Physica Medica 80 (2020) 251–258. doi:https://doi.org/10.1016/j.ejmp.2020.10.031.
URL https://www.sciencedirect.com/science/article/pii/S112017972030274X

[18] F. Sutanto, T. M. Classen, S. A. Dazeley, M. J. Duvall, I. Jovanovic, V. A. Li, A. N. Mabe, E. T. E. Reedy, T. Wu, SANDD: A directional antineutrino detector with segmented ^{6}Li-doped pulse-shape-sensitive plastic scintillator, Nucl. Instrum. Meth. A 1006 (2021) 165409. arXiv:2105.00083, doi:10.1016/j.nima.2021.165409.

[19] J. Steele, J. Brown, E. Brubaker, K. Nishimura, SCEMA: a high channel density electronics module for fast waveform capture, Journal of Instrumentation 14 (02) (2019) P02031–P02031. doi:10.1088/1748-0221/14/02/p02031.
URL https://doi.org/10.1088/1748-0221/14/02/p02031

[20] Eljen Technology, General purpose plastic scintillator EJ-200, EJ-204, EJ-208, EJ-212, https://eljentechnology.com/images/products/data_sheets/EJ-200_EJ-204_EJ-208_EJ-212.pdf, accessed: September 2021 (Sep. 2021).

[21] Eljen Technology, Silicone rubber optical interface EJ-560, https://eljentechnology.com/images/products/data_sheets/EJ-560.pdf, accessed: July 2021 (Jul. 2021).

[22] Eljen Technology, Silicone grease EJ-550, EJ-552, https://eljentechnology.com/images/products/data_sheets/EJ-550_EJ-552.pdf, accessed: July 2021 (Jul. 2021).

[23] M. Bitossi, R. Paoletti, D. Tescaro, Ultra-fast sampling and data acquisition using the DRS4 waveform digitizer, IEEE Transactions on Nuclear Science 63 (4) (2016) 2309–2316. doi:10.1109/tns.2016.2578963.
URL https://doi.org/10.1109/tns.2016.2578963

[24] BK Precision, Triple output programmable dc power supply, https://bkpmedia.s3.amazonaws.com/downloads/datasheets/en-us/9129B_datasheet.pdf, accessed: October 2021 (Oct. 2021).

[25] R. Brun, F. Rademakers, ROOT — an object oriented data analysis framework, Nuclear Instruments and Methods in Physics Research Section A: Accelerators, Spectrometers, Detectors and Associated Equipment 389 (1-2) (1997) 81–86. doi:10.1016/s0168-9002(97)00048-x.
URL https://doi.org/10.1016/s0168-9002(97)00048-x

[26] SensL Technologies Ltd., ArrayJ series: Silicon photomultiplier (SiPM) high fill-factor arrays, https://www.onsemi.com/pub/Collateral/ARRAYJ-SERIES-D.PDF, accessed: July 2021 (Jan. 2019).

[27] Photek Limited, LPG-405 pulsed laser for time-resolved detector diagnostics, https://www.photek.com/pdf/datasheets/electronics/DS036-LPG-405-Datasheet-issue-2.pdf, accessed: July 2021 (Dec. 2017).

[28] Stanford Research Systems, Model DG535 digital delay / pulse generator, https://www.thinksrs.com/downloads/pdfs/manuals/DG535m.pdf, accessed: July 2021 (Apr. 2017).

[29] L. Lista, Combination of measurements and the BLUE method, EPJ Web of Conferences 137 (2017) 11006. doi:10.1051/epjconf/201713711006.
URL https://doi.org/10.1051/epjconf/201713711006